



Highly visible-light active nanoporous TiO₂ photocatalysts for efficient solar photocatalytic applications

Hyun Uk Lee^{a,*}, Soon Chang Lee^a, Sae Hae Choi^b, Byoungchul Son^c, Soo Jae Lee^b,
Hae Jin Kim^a, Jouhahn Lee^{c,*}

^a Division of Materials Science, Korea Basic Science Institute, Daejeon 305-333, Republic of Korea

^b College of Pharmacy, Chungbuk National University, Cheongju 361-763, Republic of Korea

^c Jeonju Center, Korea Basic Science Institute, Jeonju 561-756, Republic of Korea

ARTICLE INFO

Article history:

Received 4 July 2012

Received in revised form 29 August 2012

Accepted 9 September 2012

Available online 15 September 2012

Keywords:

Titanium dioxide

Photocatalyst

Sol–gel method

Photocatalytic activity

ABSTRACT

We report highly visible-light active nanoporous carbon-doped TiO₂ (C-TiO₂) and sulfur-doped TiO₂ (S-TiO₂) for environmental and biomedical applications. C-TiO₂ and S-TiO₂ were synthesized at room temperature without thermal treatment using modified sol–gel processing and ultrasound irradiation. Under visible-light irradiation, the highest photocatalytic activity for S-TiO₂ ($[k] = 3.121 \text{ h}^{-1}$) was found to be 28 times higher than that of undoped nanoporous TiO₂ ($[k] = 0.112 \text{ h}^{-1}$). The recyclability of the S-TiO₂ photocatalyst was found to be high with the decolorization rate at ~92% of the initial value after fifteen cycles. Very interestingly, the C-TiO₂ and S-TiO₂ photocatalysts (crystallite size ~5.5 nm) showed very strong antimicrobial properties against both Gram-negative *Escherichia coli* (*E. coli*) and Gram-positive *Staphylococcus aureus* (*S. aureus*) compared to 5 nm anatase TiO₂ and undoped TiO₂ photocatalysts after visible-light exposure for 3 h. More than ~95% of *E. coli* was killed, even after ten cycles of use for the S-TiO₂ photocatalyst. Thus, we have demonstrated that C-TiO₂ and S-TiO₂ can serve as multifunctional generic bactericides, as well as highly visible-light active photocatalysts.

© 2012 Elsevier B.V. All rights reserved.

1. Introduction

Photocatalytic activities at the surface of titanium dioxide (TiO₂) have attracted much attention in view of their practical applications to water and air purification, bactericidal agents, water splitting, and conversion of solar energy to electrical and chemical energy because of its good chemical and photonic stability, and relatively good reactivity [1–5]. To improve the photocatalytic activity of TiO₂, one would like (1) a high crystallinity, (2) a narrower band gap to utilize ultraviolet (UV)/visible-light energy, (3) a large surface area to increase the density of active sites available for surface reactions, and (4) enhanced interfacial charge carrier transfer rate [6–8].

The development of photocatalysts that show high activity under visible-light irradiation ($\lambda > 400 \text{ nm}$) is needed in order to utilize artificial sun-light more effectively in photocatalytic activities [9]. In order to utilize a wider range of solar energy, many efforts have been made to narrow the band-gap by doping TiO₂ with transition metals (Cu, Co, Ni, Cr, Mn, Mo, Nb, V, Fe, Ru, Au, Ag, and Pt) [10–18], and reduced forms of TiO_x photocatalysts have also been investigated [19]. Treatment of TiO₂ powder with hydrogen

peroxide [20] or chelating agents [21,22] also allows some photocatalytic activities under visible-light irradiation. Recently, many researchers have reported that TiO₂ doped with nonmetals (C, S, N, and F) shows photoabsorption at wavelengths longer than 400 nm [23–27]. This would allow the use of visible-light in photochemistry and photocatalysis, with important and beneficial fallout on the environment, energy, and bio-medical applications [28–30].

Traditional methods for the preparation of nonmetal-doped TiO₂ photocatalysts include high temperature sintering of a nonmetal-containing TiO₂ precursor [31–34], chemical vapor deposition (CVD) or pyrolysis [35–37], gas phase [24,26], and solution phase strategies [25,27–30,38–41]. However, these methods generally require subsequent thermal treatment (up to 400 °C) for crystallization of the amorphous and semicrystalline TiO₂. Thermal treatments required for the preparation of nonmetal-doped TiO₂ are costly and make large-scale application difficult [31,42]. Hence, nanocrystalline TiO₂ has been synthesized at low temperature and several research studies have been carried out to broaden the optical response range by doping TiO₂ with nonmetals [31,43–46]. However, it is still a challenge to synthesize nonmetal-doped TiO₂ at room or low temperature, especially for visible-light active photocatalysts with efficient solar photocatalytic activities in large scale for pollutant removal and bactericidal effects.

* Corresponding author. Tel.: +82 42 865 3637; fax: +82 42 865 3610.
E-mail address: leeho@kbsi.re.kr (H.U. Lee).

In this work, we show that nanoporous C-doped TiO₂ (C-TiO₂) and S-doped TiO₂ (S-TiO₂) with anatase crystallinity were synthesized at room temperature (RT) without thermal treatment by using modified sol–gel processing and ultrasound irradiation. Ultrasound irradiation aids in crystallizing C-TiO₂ and S-TiO₂, stabilizing their nanoporous structures and removing the organic components [47–49]. The C-TiO₂ and S-TiO₂ with high crystallinity (pure anatase phase) and large surface area (C-TiO₂: 465.3 m²/g; S-TiO₂: 485.2 m²/g) exhibited very high photocatalytic activity toward the oxidation of azo dyes [reactive black 5 (RB 5) and rhodamine B (Rho B)], and efficient sterilization (or killing) of bacteria [Gram-negative *Escherichia coli* (*E. coli*) and Gram-positive *Staphylococcus aureus* (*S. aureus*)] under visible-light irradiation. The photocatalytic and antibacterial activities of the C-TiO₂ and S-TiO₂ samples were higher than those of the commercial 5-nm anatase TiO₂ catalyst particles (5 nm a-TiO₂) and undoped nanoporous TiO₂ photocatalyst (TiO₂).

2. Experimental

2.1. Synthesis of TiO₂ photocatalyst

Titanium *n*-butoxide (TBOT; Ti(OCH₂CH₂CH₂CH₃)₄, 97%), dodecyltrimethyl ammonium bromide [CH₃(CH₂)₁₁N(CH₃)₃Br], methanol (CH₃OH, 99.8%), sulfuric acid (H₂SO₄, 37%), and hydrogen peroxide (H₂O₂, 30%) were used as-received from Sigma–Aldrich Co., without further purification. In a typical synthesis, 0.056 mol TBOT and 0.01 mol dodecyltrimethyl ammonium bromide were dissolved in 1000 mL deionized water and the mixture was vigorously stirred for 5 min at RT. After 6 h aging, the white precipitate was filtered, washed five times with ethanol-deionized water solution (50:50, v/v%), and finally dried under air at RT [50]. After 20 g of dried TiO₂ powder was dissolved in 1000 mL of deionized water (pH 4), this mixture was treated with high-intensity ultrasound with a frequency of 20 kHz which was applied from the top of the glass reactor using a Sonics & Materials, Inc. VC 750 ultrasonic generator (13 mm diameter high-intensity probe, amplitude 50%). Ultrasound irradiation was just applied for 40 min, with the electrical energy input maintained at 100 W/cm². The mixture was filtered; the resultant TiO₂ powder was washed several times with ethanol-deionized water, and finally dried under vacuum at RT.

2.2. Synthesis of carbon-doped TiO₂ (C-TiO₂) photocatalyst

Dried TiO₂ powder (20 g) was dispersed in 1000 mL methanol–water solution (80:20 methanol–water) and vigorously stirred for 5 min at RT. Ultrasound irradiation was just applied for 40 min, with the electrical energy input maintained at 100 W/cm². The yellowish TiO₂ powder (C-TiO₂) was filtered, washed five times with deionized water, and finally dried under air at RT.

2.3. Synthesis of sulfur-doped TiO₂ (S-TiO₂) photocatalyst

Dried TiO₂ powder (20 g) was dispersed in 900 mL of 1 M H₂SO₄ solution and H₂O₂ solution (100 mL) was added dropwise with vigorous stirring for 5 min at RT. Ultrasound irradiation was just applied for 40 min, with the electrical energy input maintained at 100 W/cm². The orange-red colored TiO₂ powder was filtered, washed five times with deionized water, and finally dried under air at RT.

2.4. Characterization

The crystalline structures of the 5 nm a-TiO₂, as-grown TiO₂, TiO₂, C-TiO₂, and S-TiO₂ photocatalysts were investigated by X-ray

diffraction (XRD; Rigaku RDA-CA X-ray diffractometer, Japan) using Cu K α radiation with a nickel filter. The morphologies and size distributions of the as-grown TiO₂, TiO₂, C-TiO₂, and S-TiO₂ photocatalysts were evaluated with a field emission-scanning electron microscope (FE-SEM; Hitachi S-4700, Japan) and high resolution-transmission electron microscope (HR-TEM; JEOL JEM 2200, Japan). Before analysis, the samples were placed onto the surfaces of copper grids and dried under ambient conditions. The Brunauer–Emmett–Teller (BET) surface area, pore volume, and pore diameter of the as-grown TiO₂, TiO₂, C-TiO₂, and S-TiO₂ photocatalysts were determined using a BET analyzer (Micromeritics ASAP 2020, USA). High resolution X-ray photoelectron spectroscopy (HR-XPS) with monochromatic Al K α X-ray radiation ($h\nu$ = 1486.6 eV) operated at 120 W (Kratos Analytical, AXIS Nova, UK) was used to investigate the surface properties of the samples. The shift of the binding energy due to relative surface charging was corrected using the C1s level at 284.6 eV as an internal standard. The depth profiling XPS was performed with Ar⁺ ion bombardment. The beam voltage is 3 kV, the beam density is 6 nA/cm², and the sputter area is 4 mm \times 4 mm. A He–Cd laser (Kimmon, 1K, Japan) with a wavelength of 325 nm and a power of 50 mW was utilized as an excitation source for Photoluminescence (PL) measurements using a spectrograph (f = 0.5 m, Acton Research Co., Spectrograph 500i, USA) with an intensified CCD (PI-MAX3, Princeton Instruments, IRY1024, USA).

2.5. Measurement of photocatalytic and antibacterial activity

The photocatalytic degradations of RB 5 (3 mg/L, pH 6.67, Aldrich, USA) and Rho B (3 mg/L, pH 5.5, Aldrich, USA) solutions by the catalyst samples (0.5 g/L) were carried out under UV (source: 4 W, 365 nm, VSLAB VL-4CL, Korea) and visible-light (source: 150 W Xe lamp, 425 nm $>$ λ , SCHOTT, USA) irradiation, and the absorbance of the solutions was measured using a UV-Vis-NIR spectrophotometer (Varian, Cary 5000, Australia) in the region 200–800 nm. The concentrations of RB 5 and Rho B in the solutions after photo-irradiation were measured from the peak intensities of the absorbance of the solutions at 598 and 555 nm, respectively [51]. The changes in the concentration [$\ln(C_0/C) = kt$, where k is the apparent reaction rate constant, and C_0 and C are the initial and reaction concentrations of RB 5 or Rho B] of the dye solution with reaction time for the samples were also investigated. Evolved CO₂ was analyzed with a TM IGC120-MB gas chromatograph equipped with a Q column. To demonstrate the stability of the photocatalysts, we recycled the used S-TiO₂ for testing other photocatalytic activities. The recycling tests of the photocatalytic activity of S-TiO₂ were performed after washing three times with 3 deionized water (3 DW) and drying in an oven for 6 h after each cycle. Action spectrum analysis was carried out for photocatalytic reaction under monochromatic light irradiation using a JASCO CRM-FD diffraction grating-type illuminator. The apparent quantum yield was calculated as a ratio of RB 5 decomposition rate.

The antibacterial activities of the samples were evaluated by the inhibition of *E. coli* and *S. aureus* under conditions of visible-light irradiation. Before the antibacterial activity tests, all glassware and samples were sterilized by autoclaving at 120 °C for 15 min. Bacterial cultures were grown in LB media overnight at 37 °C with continuous shaking at \sim 200 rpm. The treated bacterial cells were diluted to a cell suspension of $\sim 2 \times 10^5$ colony-forming units (CFUs)/mL with deionized water. The mass of the photocatalyst was adjusted to 25 μ g/mL. The mixture suspensions were stirred with a magnetic stirrer to prevent the samples from settling and exposed to visible-light irradiation (420 nm $>$ λ $>$ 700 nm, 150 W) at various irradiation times (0, 30, 60, 90, 120, 150, and 180 min). Then, 1 mL of mixture suspension was sampled, added to the LB plate,

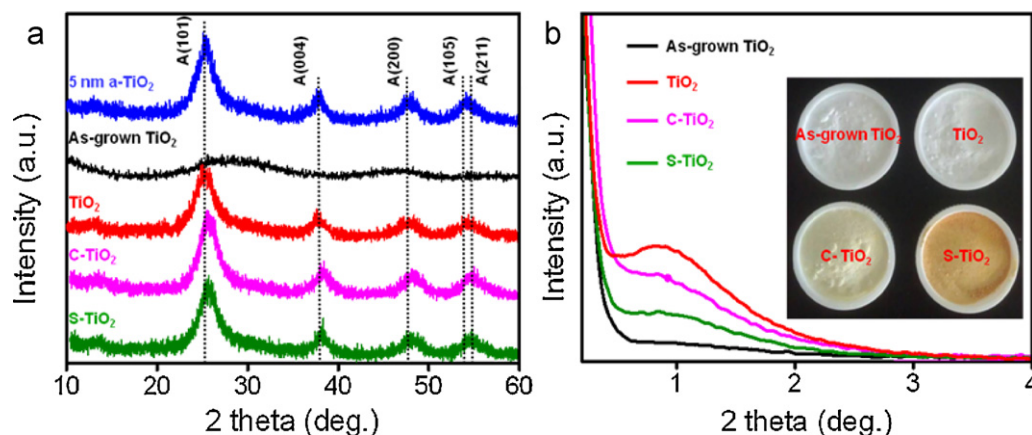


Fig. 1. (a) Wide-angle and (b) small-angle XRD patterns of the 5 nm a-TiO₂, as-grown TiO₂, TiO₂, C-TiO₂, and S-TiO₂ photocatalysts. The peaks are identified as anatase (A). The inset shows pictures of the as-grown TiO₂, TiO₂, C-TiO₂, and S-TiO₂ photocatalysts.

and incubated overnight at 37 °C. After incubation, the bacterial colonies were observed and quantified [52–54].

For the photocatalytic activity and antimicrobial tests, the data were averaged and expressed as the mean \pm standard deviation. Each test was repeated up to five times. Statistical analysis was performed using analysis of variance (ANOVA), with p -values < 0.05 considered as significant.

3. Results and discussion

3.1. Physicochemical, structural and optical properties of C- and S-TiO₂ photocatalysts

A XRD studies were carried out to investigate the crystal identity of the TiO₂ samples and the effect of C and S doping on the crystal structure of TiO₂ (Fig. 1). Fig. 1a shows the wide-angle XRD patterns of the 5 nm a-TiO₂, as-grown TiO₂, TiO₂, C-TiO₂, and S-TiO₂ photocatalysts. The intensities and positions of the observed peaks are in agreement with literature values (JCPDS 73-1764). The obtained XRD patterns of the as-grown TiO₂ clearly show a phase transition from amorphous to the anatase crystal structure after ultrasound irradiation (TiO₂). The high-intensity ultrasound irradiation induces better crystallization (pure anatase phase) of TiO₂, because ultrasonic cavitations create a unique environment [47–49]. No characteristic peaks were observed for other phase types (i.e., rutile or brookite), indicating the high purity and crystallinity of TiO₂ formed via our method. From these patterns, it was found that the 5 nm a-TiO₂, TiO₂, C-TiO₂, and S-TiO₂ samples were the anatase phase, and the C-TiO₂ and S-TiO₂ samples have a clear peak broadening because of the higher crystallite size of the TiO₂ nanoparticles versus that of TiO₂. The average crystallite sizes of anatase TiO₂ were calculated from the Debye–Scherrer equation by using the main (1 0 1) diffraction peak of TiO₂ anatase [55], and it was found that the average crystallite sizes of anatase TiO₂, C-TiO₂, and S-TiO₂ were 5.3, 5.8, and 5.5 nm, respectively. It is clear that the diffraction peaks of the C-TiO₂ and S-TiO₂ samples shifted to higher diffraction angles (~ 0.4 eV) compared with those of TiO₂. The results imply that an oxygen atom in the TiO₂ lattice is substituted by a carbon or sulfur atom.

The broadening of the diffraction peak of TiO₂ in the low-angle XRD patterns indicated the presence of a randomly nanoporous structure, as shown in Fig. 1b. The considerable broadening and reduction in the intensity of this peak in the C-TiO₂ and S-TiO₂ can be attributed to the partial shrinkage or collapse of the nanoporous

structure caused by the increased average crystallite sizes of C-TiO₂ and S-TiO₂.

The surface morphologies of the as-grown TiO₂, TiO₂, C-TiO₂, and S-TiO₂ photocatalysts were probed using a FE-SEM (Fig. S1). The diameters of the TiO₂ particles (~ 27 nm) were found to be 1.4 times smaller than those of as-grown TiO₂ aggregated particles (~ 40 nm), because of the degradation of the cationic surfactant [dodecyltrimethyl ammonium bromide; CH₃(CH₂)₁₁N(CH₃)₃Br] by the unique conditions of ultrasound irradiation (Fig. S1) [47–49]. The small aggregates of the TiO₂, C-TiO₂, and S-TiO₂ samples resulted in their morphological change to randomly shaped aggregated particles. They consist of inter-grown fundamental TiO₂ nanoparticles with rough and uneven surfaces. The inter-growth of small primary particles results in aggregates with significant extra-framework void space, which is consistent with the textural nanoporosity observed in the BET results (Table S1), and because it is the nanoporous structure that is formed by the aggregation of particles with sizes of several nanometers.

In order to investigate the properties of the C-TiO₂ and S-TiO₂, HR-TEM images were obtained, as shown in Fig. 2. The pore structure comprising the nanoporous framework was composed of inter-connected TiO₂ nanoparticles (Fig. 2a and c). The HR-TEM images further revealed that the pore walls consisted of aggregated nanocrystalline anatase with average crystallite sizes of ~ 5.7 nm (C-TiO₂) and ~ 5.5 nm (S-TiO₂) (Fig. 2b and d). The crystallite sizes obtained from the HR-TEM results were consistent with the XRD values. The crystallites had sets of clearly resolved lattice fringes, thus proving that the crystallinity of the C-TiO₂ and S-TiO₂ samples was high. Electron diffraction patterns of the C-TiO₂ and S-TiO₂ samples were observed in a selected area of electron diffraction (SAED, inset, Fig. 2b and d), which were (1 0 1), (0 0 4), (2 0 0), (1 0 5), and (2 0 4) diffractions of the polycrystals with the anatase phase [28,56]. The HR-TEM images and XRD patterns therefore indicated that the C-TiO₂ and S-TiO₂ samples consisted of nanoporous structures with the anatase crystal phase. The observed spacing between the lattice planes of both samples was obtained as 0.35 nm, corresponding to the (1 0 1) plane of the anatase crystal [28].

The HR-XPS measurements were carried out to further investigate the chemical state of the C-TiO₂ and S-TiO₂ samples (Fig. 3). The HR-XPS spectra of C1s in the surfaces of TiO₂ and C-TiO₂ are shown in Fig. 3a. After doping, four peak structures were observed at the binding energies of 282.6, 284.6, 286.1, and 288.3 eV [57]. The peak at 284.6 eV could possibly be the signal from carbon tape and free carbon in the samples [53,54]. A main contribution at 284.6 eV was ascribed to C1s, while contributions at 286.1 and 288.3 eV

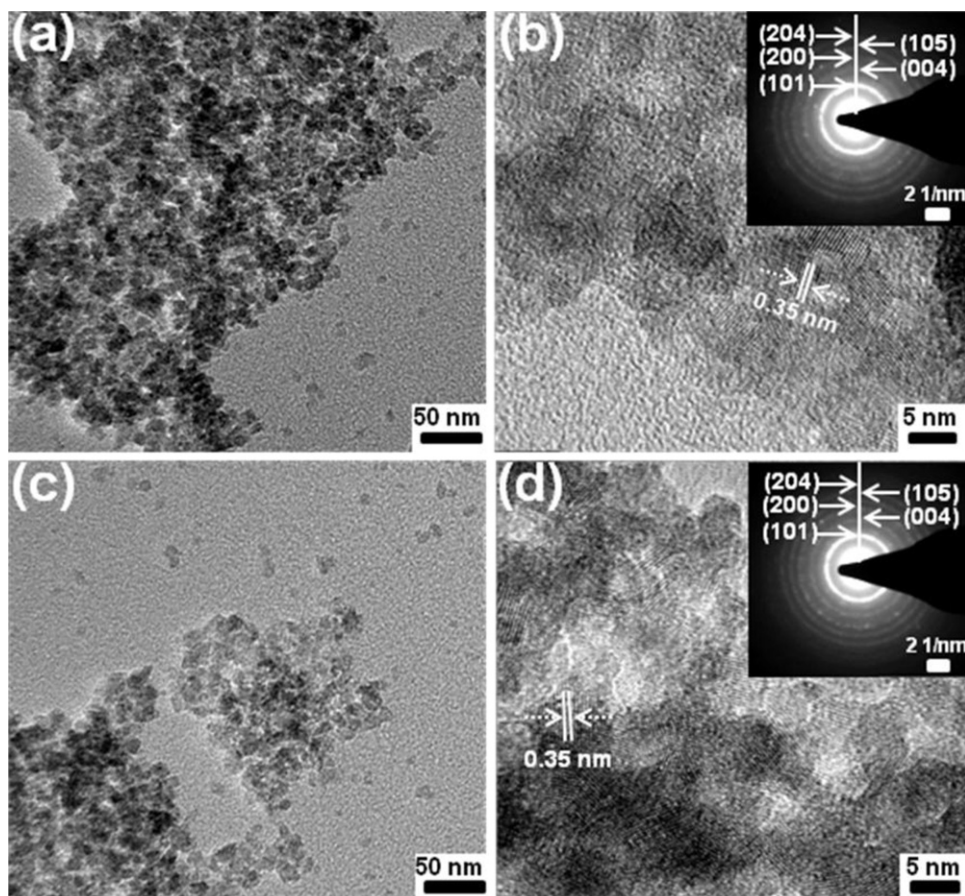


Fig. 2. HR-TEM images of the C-TiO₂ (a and b) and S-TiO₂ (c and d) photocatalysts at different magnifications.

were due to the C–O(H) and C=O, respectively [43,58]. The peak around 282.6 eV was ascribed to the existence of O–Ti–C bonds [57]. The peak at 286.1 eV indicated the presence of C–O bonds, and the carbon might substitute for some of the lattice titanium atoms to form a Ti–O–C structure. Obviously, the doping carbon species in C-TiO₂ might exist as O–Ti–C and Ti–O–C. One species substitute carbon for the oxygen of the anatase in the as-prepared photocatalysts and another species incorporates carbon into the interstitial positions of the TiO₂ lattice. Fig. 3b shows the HR-XPS

spectra of the S2p region of the TiO₂ and S-TiO₂. It can be observed that the S2p peaks around 167.4 eV and 168.5 eV are shifted negatively by 0.5 eV in comparison with the standard binding energy of the sulfur in pure SO₃²⁻ (167.9 eV) and SO₄²⁻ (169.0 eV), which was proved by another research groups [59–61]. The sulfur atoms are all in the state of S²⁻, with a peak at approximately 160–163 eV [60,61]. This corresponds to the Ti–S bond formed when some of the oxygen atoms in the TiO₂ lattice are replaced by sulfur atoms. Anionic sulfur doping may be difficult to carry out because the

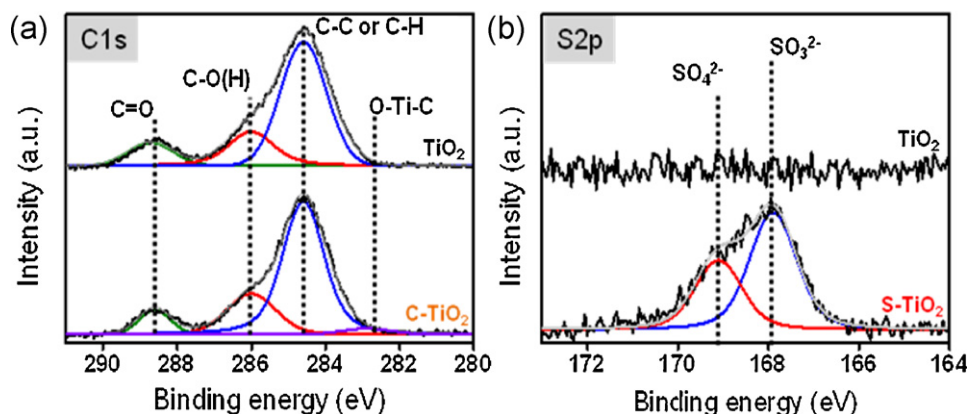


Fig. 3. (a) C1s and (b) S2p HR-XPS spectra of the TiO₂, C-TiO₂, and S-TiO₂ photocatalysts.

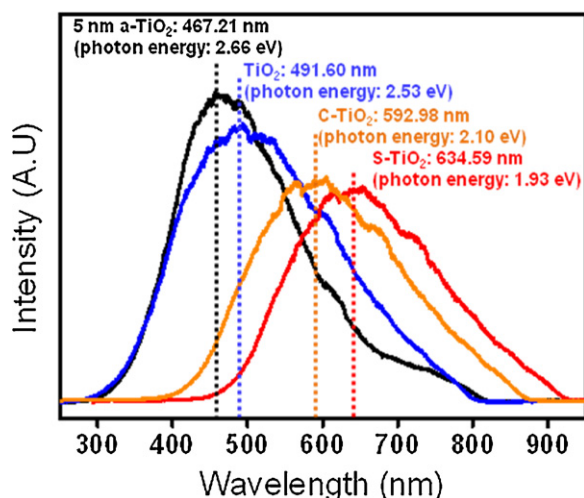


Fig. 4. PL spectra of the 5 nm a-TiO₂, TiO₂, C-TiO₂, and S-TiO₂ photocatalysts.

ionic radius of S²⁻ (1.7 Å) is significantly larger compared to that of O²⁻ (1.22 Å) [59–62]. This leads to the large formation energy required for substitutionally forming Ti–S bonds instead of Ti–O bonds. Thus, the substitution of Ti⁴⁺ by S⁶⁺ is chemically more favorable than replacing O²⁻ with S²⁻, and consequently, Ti–O–S bonds form. The samples were characterized by depth profiling XPS to clarify changes in chemical state and atomic ratio with sputtering depth as shown in Fig. S2. The atomic ratio of C (C-TiO₂) and S (S-TiO₂) decreases slightly with sputtering time increasing.

PL emission spectra have been widely used to investigate the efficiency of charge carrier trapping, migration, and transfer in order to understand the fate of electron–hole pairs in semiconductor particles, since PL emission results from the recombination of free carriers [59,63,64]. In this study, the TiO₂ sample showed a broad PL emission peak located around 491.60 nm, as shown in Fig. 4. However, broad visible PL bands centered at 592.98 and 634.59 nm can be observed for the C-TiO₂ and S-TiO₂ samples, respectively. It can be seen from Fig. 4 that the PL intensity of TiO₂ is much higher than those in the spectra of the C-TiO₂ and S-TiO₂ samples, indicating that C and S doping can effectively inhibit the recombination of excited electrons and holes [63,64]. Further inspection of Fig. 4 reveals a 101.38 (C-TiO₂) and 142.99 nm (S-TiO₂) shift of the emission peaks toward longer wavelengths when nonmetals are doped into TiO₂ photocatalysts. The emission signals at 592.98 and 634.59 nm may originate from the charge-transfer transition from oxygen vacancies to new energy levels caused by

nonmetal (C and S) doping. This effective quenching of the photoluminescence can be attributed to two pathways [63,64]: (1) the excited electron is trapped by the oxygen vacancy, whereas the hole is trapped by the doped C and S, which reduces the recombination rate; (2) the excited electron can transfer from the valence band to the new defect levels introduced by C and S doping that exist near the conduction band minimum which can also decrease the PL intensity.

3.2. Photocatalytic activity of C- and S-TiO₂ photocatalysts

The photocatalytic activities of the TiO₂ samples were evaluated by measuring the decomposition rate of RB 5 and Rho B solutions under UV irradiation (Fig. 5). RB 5 was hardly degraded without a photocatalyst under UV irradiation, and the color removal of the dye was only 1.7% under UV irradiation for 70 min. With the C-TiO₂ and S-TiO₂ photocatalysts prepared by our methods, 100% color removal of the dye solution occurred after UV irradiation for 70 min. The activity orders of the 5 nm a-TiO₂ and TiO₂ samples are in good agreement with their corresponding PL intensity orders; in other words, the stronger the PL signal, the lower the photocatalytic activity, which indicates that catalysts with stronger PL signals could act as recombination centers for electron–hole pairs. The superior activity of the C-TiO₂ and S-TiO₂ samples can be ascribed to their higher BET surface areas (Table S1) and lower PL signals (Fig. 4). Larger specific surface area allows more gaseous reactants to be adsorbed onto the surface of the photocatalyst [65,66]. The lower PL signal indicates a higher separation rate of electron–hole pairs which was caused by nonmetal doping [63,64]. All of these factors contributed to enhanced photocatalytic activity. However, it should be noted that TiO₂ had a larger surface area (502.7 m²/g) than C-TiO₂ and S-TiO₂, yet its photocatalytic activity was lower than that of C-TiO₂ and S-TiO₂. This fact can be attributed to the faster recombination rate of electron–hole pairs and lower anatase crystallinity of TiO₂ [65,66].

Under visible-light irradiation, distinct photocatalytic activities of the 5 nm a-TiO₂, TiO₂, C-TiO₂, and S-TiO₂ were observed, as shown in Fig. 6. Both 5 nm a-TiO₂ and TiO₂ exhibit almost no visible-light activity due to the fact that the TiO₂ photocatalyst has band-gap energy of approximately 3 eV [1–5]. After C and S atoms are doped into the TiO₂ photocatalysts, the visible-light photocatalytic activities of the prepared samples increased greatly. The 5 nm a-TiO₂ and TiO₂ showed very poor photocatalytic activities under visible-light. However, with the C-TiO₂ and S-TiO₂, the color removal of the dye solution was found to be 99% under visible-light irradiation for 70 min. The highest degradation rate for S-TiO₂ ($k = 3.121 \text{ h}^{-1}$) was 28 times faster than that of TiO₂

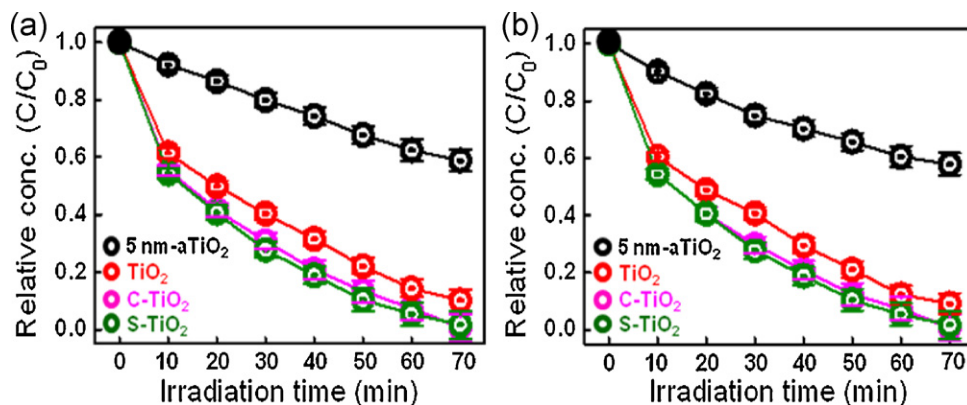


Fig. 5. Comparison of the photocatalytic behavior of the 5 nm a-TiO₂, TiO₂, C-TiO₂, and S-TiO₂ photocatalysts in the decomposition of (a) RB 5 and (b) Rho B dye solutions under UV irradiation.

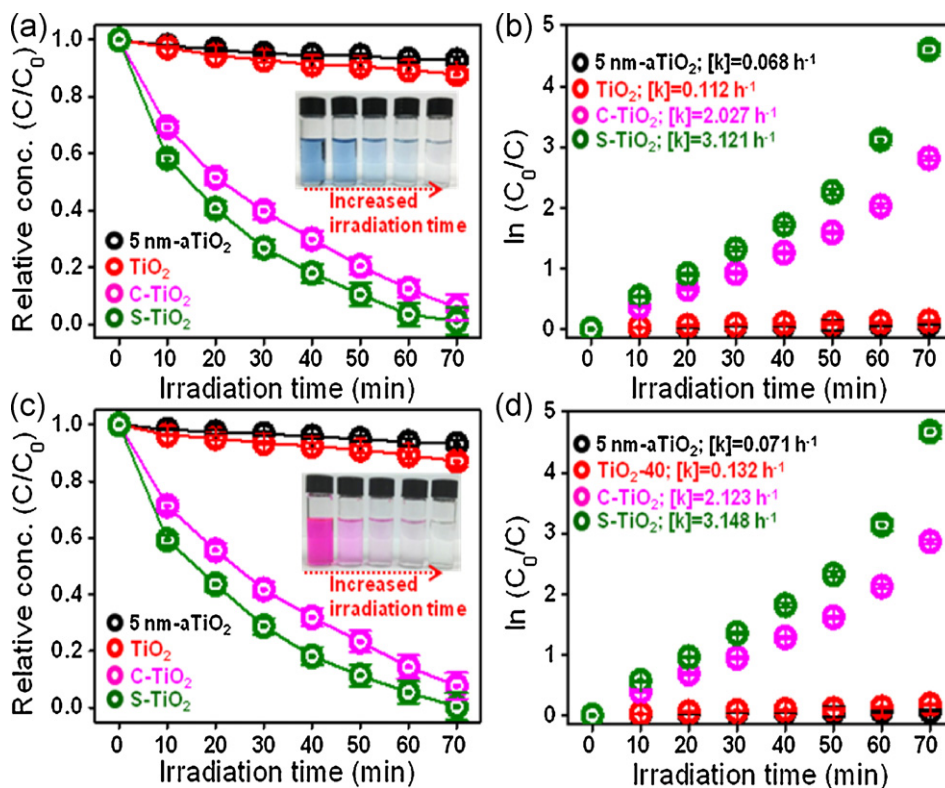


Fig. 6. Comparison of the photocatalytic behavior of the 5 nm a-TiO₂, TiO₂, C-TiO₂, and S-TiO₂ photocatalysts in the decomposition of RB 5 (a and b) and Rho B (c and d) dye solutions under visible-light irradiation. The data were fitted as dotted lines and the corresponding decomposition rates (k) are given.

($k = 0.112 \text{ h}^{-1}$). As shown above, the C and S doping may possibly generate an intermediate energy level above the valence band of TiO₂, thereby narrowing the band-gap to induce visible-light absorption [59]. These results demonstrate that the C-TiO₂ and S-TiO₂ could be effective visible-light driven and higher activity photocatalysts.

The quantity of evolved CO₂ during the photocatalytic reaction of RB 5 with TiO₂ photocatalysts under visible-light irradiation is shown in Fig. 7a. The evolved CO₂ increased gradually as the photocatalytic reaction progressed. After visible-light irradiation of 70 min, the quantity of evolved CO₂ for S-TiO₂ (0.214 mmol) was 30 times higher than that of TiO₂ (0.007 mmol). These results show that a high degree of mineralization for RB 5 was achieved. The length of visible-light irradiation for one cycle was 70 min, and decolorization was measured at the end of each cycle (Fig. 7b).

After fifteen runs of the degradation reaction, the photocatalytic conversion ratio of RB 5 for the S-TiO₂ photocatalyst remained approximately 92% under visible-light irradiation. The decrease in the photocatalytic conversion ratio after every cycle was most likely due to the loss of the S-TiO₂ photocatalyst. However, we can clearly see that the removal efficiency of organic contaminants using S-TiO₂ remained approximately constant, even after fifteen cycles. Undoubtedly, the S-TiO₂ also exhibits excellent photocatalytic stability.

Fig. 8 shows the action spectra of the TiO₂ photocatalysts. Obviously, compared to the 5 nm a-TiO₂ or TiO₂, the action region of C-TiO₂ and S-TiO₂ extended significantly into the visible-light region. This action spectra strongly suggest that the C-TiO₂ and S-TiO₂ photocatalysts can be activated by visible-light. Therefore, this illustrates that the presence of sulfur (or carbon) not only enhances

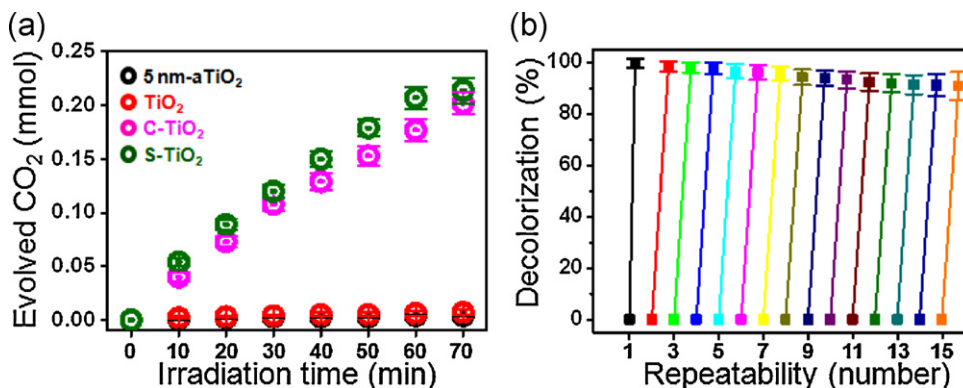


Fig. 7. (a) Evolution of CO₂ from reactive black 5 (RB 5) as a function of visible-light irradiation time (min) by photocatalytic reaction with TiO₂ photocatalysts, and (b) recycling results of the S-TiO₂ photocatalyst in the decolorization of RB 5 solution.

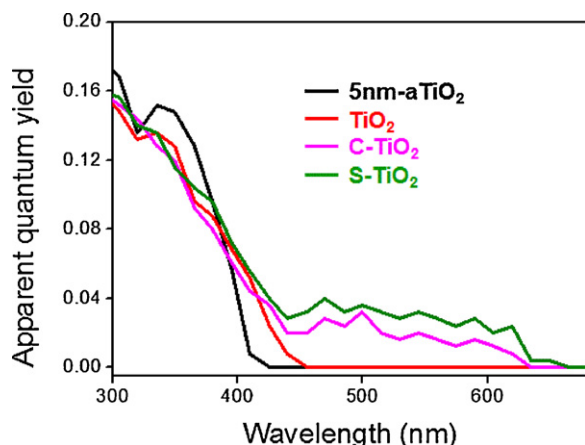


Fig. 8. Action spectra of RB 5 decomposition on TiO₂ photocatalysts in overall region.

photocatalytic performance in the degradation of organic dye pollutants for TiO₂, but also exhibits excellent photocatalytic stability in the visible-light range.

3.3. Antibacterial activities of C- and S-TiO₂ photocatalysts

The antibacterial activities of the C-TiO₂ and S-TiO₂ in the disinfection of *E. coli* under visible-light irradiation were compared with 5 nm a-TiO₂ and TiO₂, according to the decrease in the colony numbers of *E. coli* and *S. aureus* formed on LB plates (Fig. 9). C-TiO₂ and S-TiO₂ inhibited the growth of *E. coli* and *S. aureus* efficiently, and their antibacterial activities became stronger with increased visible-light irradiation times. The bacterial survival was calculated by % survival = $B/A \times 100$ (where the numbers of surviving microbial colonies under the non-irradiated and visible-light irradiated conditions were A and B, respectively). For the TiO₂, ~10% bacterial inhibition of *E. coli* bacteria was observed after 180 min visible-light irradiation. After 30 min irradiation, the 5 nm a-TiO₂ exhibited 98.3% survival, whereas S-TiO₂ (47.4% survival) was nearly twice as active against *E. coli*. This is possibly due to the higher concentration of OH radicals, which are very strong oxidant species with antimicrobial activity, on the surface of S-TiO₂ under visible-light irradiation conditions [62,67]. According to Fig. 9, *E. coli* can be almost completely killed within 180 min on C-TiO₂ and S-TiO₂ under visible-light irradiation. A similar result was observed in the antibacterial test against *S. aureus*. The results indicate that C-TiO₂ and S-TiO₂ exhibited higher antibacterial activities compared to 5 nm a-TiO₂ and TiO₂ when exposed to visible-light. Moreover, S-TiO₂ had good stability, as demonstrated by the recycle runs

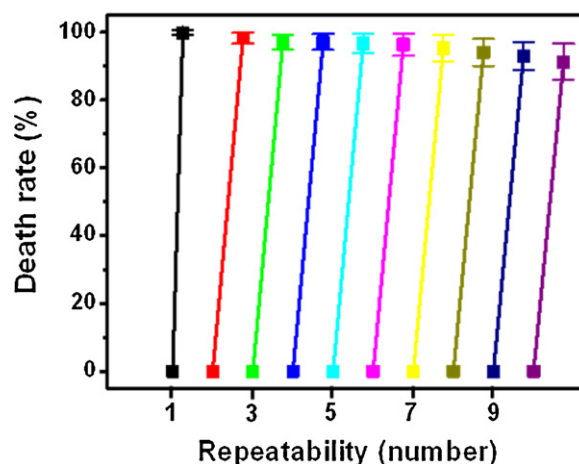


Fig. 10. The biocidal efficacy of the S-TiO₂ photocatalyst against *E. coli*.

(Fig. 10). After ten consecutive tests, the kill percentages of the bacteria were still as high as ~95% for *E. coli*. The S-TiO₂ was found to be strong enough to withstand the recyclability test. This excellent antibacterial activity under visible-light can be applied to many useful applications for alternative sterilization technology.

3.4. Highly visible-light photocatalytic and antibacterial activities of C- and S-TiO₂ photocatalysts

The highly visible-light photocatalytic and antibacterial activities of C-TiO₂ and S-TiO₂ can be attributed to the following factors: (1) better anatase crystallinity. The TiO₂ with higher anatase crystallinity is an important factor that enhances its effective utilization to improve photocatalytic activity [68,69]. (2) A narrower band-gap. It is possible that the C or S may substitute for some of the lattice titanium atoms close to/on the surface of TiO₂ because the TiO₂ was already formed before doping. Therefore, band-gap narrowing occurred in the C-TiO₂ and S-TiO₂, which could absorb more visible-light [59,65,66]. (3) Decrease of electron-hole pairs. The lower intensity of the visible PL bands of C-TiO₂ and S-TiO₂ indicate the enhancement of the separation of electron-hole pairs which was caused by nonmetal doping [59]. (4) Larger surface area. A large surface area allows more dye molecules to be adsorbed onto the surface of the photocatalyst, and more photocatalyst adherence to bacterial surfaces [62,65–67]. The results of the BET analysis revealed that the surface area of C-TiO₂ (465.3 m²/g) and S-TiO₂ (485.2 m²/g) was greater than that of the 5 nm a-TiO₂ (123.6 m²/g). Considering these factors, it is reasonable that C-TiO₂ and S-TiO₂

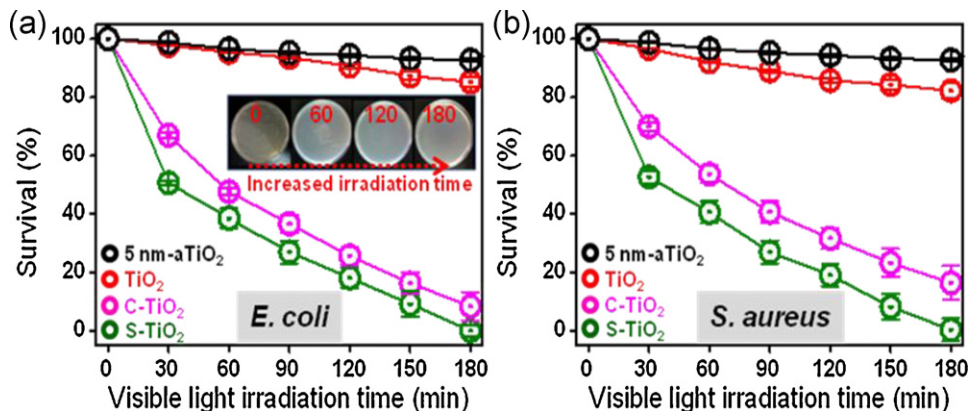


Fig. 9. Plot of survival (%) versus visible-light irradiation time (min) for the 5 nm a-TiO₂, TiO₂, C-TiO₂, and S-TiO₂ photocatalysts against (a) *E. coli* and (b) *S. aureus*.

can exhibit photocatalytic and antibacterial activities superior to those of 5 nm a-TiO₂ and TiO₂.

4. Conclusions

In summary, the nanoporous C-TiO₂ and S-TiO₂ were synthesized at RT without thermal treatment by modified sol-gel processing and ultrasound irradiation. The C-TiO₂ and S-TiO₂ with high crystallinity (pure anatase phase) and large surface areas (465.3 m²/g for C-TiO₂ and 485.2 m²/g for S-TiO₂) exhibited superior visible-light photocatalytic activity in the oxidation of azo dyes, and had good recycling properties. Moreover, C-TiO₂ and S-TiO₂ exhibited excellent antibacterial activity in the sterilization of Gram-negative *E. coli* and Gram-positive *S. aureus*. Thus, the highly visible-light active C-TiO₂ and S-TiO₂ photocatalysts with high crystallinity and large surface areas might have utility in several promising applications such as highly efficient water (or air) treatment, dye-sensitized solar cells, bactericidal agents, and self-antifouling action.

Acknowledgments

This research was supported by the Converging Research Center Program through the Ministry of Education, Science and Technology (2012K001302).

Appendix A. Supplementary data

Supplementary data associated with this article can be found, in the online version, at <http://dx.doi.org/10.1016/j.apcatb.2012.09.010>.

References

- [1] A. Kubacka, M. Fernández-García, G. Colón, Chemical Reviews 112 (2012) 1555–1614.
- [2] Y.F. Li, Z.P. Liu, Journal of the American Chemical Society 133 (2011) 15743–15752.
- [3] Z. Wang, H. Wang, B. Liu, W. Qiu, J. Zhang, S. Ran, H. Huang, J. Xu, H. Han, D. Chen, G. Shen, ACS Nano 5 (2011) 8412–8419.
- [4] P. Hartmann, D.K. Lee, B.M. Smarsly, J. Janek, ACS Nano 4 (2010) 3147–3154.
- [5] H. Tong, S. Ouyang, Y. Bi, N. Umezawa, M. Oshikiri, J. Ye, Advanced Materials 24 (2012) 229–251.
- [6] A. Fujishima, X.T. Zhang, D.A. Tryk, Surface Science Reports 63 (2008) 515–582.
- [7] X. Chen, S.S. Mao, Chemical Reviews 107 (2007) 2891–2959.
- [8] S.S. Soni, M.J. Henderson, J.F. Bardeau, A. Gibaud, Advanced Materials 20 (2008) 1493–1498.
- [9] C. Han, M. Pelaez, V. Likodimos, A.G. Kontos, P. Falaras, K. O'Shea, D.D. Dionysiou, Applied Catalysis B: Environmental 107 (2011) 77–87.
- [10] J. Zhu, J. Ren, Y. Huo, Z. Bian, H. Li, Journal of Physical Chemistry C 111 (2007) 18965–18969.
- [11] D.B. Hamal, K.J. Klabunde, Journal of Colloid and Interface Science 311 (2007) 514–522.
- [12] J. Zhu, F. Chen, J. Zhang, H. Chen, M. Anpo, Journal of Photochemistry and Photobiology A 180 (2006) 196–204.
- [13] Y.C. Nah, I. Paramasivam, P. Schmuki, ChemPhysChem 11 (2010) 2698–2713.
- [14] S.I. Shah, W. Li, C.P. Huang, O. Jung, C. Ni, Proceedings of the National Academy of Sciences U.S.A. 99 (2002) 6482–6486.
- [15] M. Anpo, M. Takeuchi, Journal of Catalysis 216 (2003) 505–516.
- [16] S. Klosek, D. Raftery, Journal of Physical Chemistry B 105 (2001) 2815–2819.
- [17] H. Haick, Y. Paz, Journal of Physical Chemistry B 107 (2003) 2319–2326.
- [18] R. Janisch, P. Gopal, N.A. Spaldin, Journal of Physics: Condensed Matter 17 (2005) R657–R689.
- [19] I. Nakamura, N. Negishi, S. Kutsuna, T. Ihara, S. Sugihara, K. Takeuchi, Journal of Molecular Catalysis A: Chemical 161 (2000) 205–212.
- [20] T. Ohno, Y. Masaki, S. Hirayama, M. Matsumura, Journal of Catalysis 204 (2001) 163–168.
- [21] S. Ikeda, C. Abe, T. Torimoto, B. Ohtani, Electrochemistry 70 (2002) 442–445.
- [22] T. Ohno, N. Murakami, T. Tsubota, H. Nishimura, Applied Catalysis A: General 349 (2008) 70–75.
- [23] D. Mitoraj, H. Kisch, Angewandte Chemie International Edition 47 (2008) 9975–9978.
- [24] S. Hoang, S. Guo, N.T. Hahn, A.J. Bard, C.B. Mullins, Nano Letters 12 (2012) 26–32.
- [25] Z. Xiong, X.S. Zhao, Journal of the American Chemical Society 134 (2012) 5754–5757.
- [26] J. Hensel, G. Wang, Y. Li, J.Z. Zhang, Nano Letters 10 (2010) 478–483.
- [27] Q. Zhang, D.Q. Lima, I. Lee, F. Zaera, M. Chi, Y. Yin, Angewandte Chemie International Edition 50 (2011) 7088–7092.
- [28] F. Dong, S. Guo, H. Wang, X. Li, Z. Wu, Journal of Physical Chemistry C 115 (2011) 13285–13292.
- [29] Q. Li, Y.W. Li, P.G. Wu, R.C. Xie, J.K. Shang, Advanced Materials 20 (2008) 3717–3723.
- [30] Y. Cong, J.L. Zhang, F. Chen, M. Anpo, D.N. He, Journal of Physical Chemistry C 111 (2007) 10618–10623.
- [31] F. Dong, H.Q. Wang, Z.B. Wu, J.F. Qiu, Journal of Colloid and Interface Science 343 (2010) 200–208.
- [32] S. Sakthivel, H. Kisch, Angewandte Chemie International Edition 42 (2003) 4908–4911.
- [33] J.H. Park, S. Kim, A.J. Bard, Nano Letters 6 (2006) 24–28.
- [34] I.N. Martynov, S. Uma, S. Rodrigues, K.J. Klabunde, Chemical Communications 7 (2004) 2476–2477.
- [35] S.U.M. Khan, M. Al-Shahry, W.B. Ingler, Science 297 (2002) 2243–2245.
- [36] G. Wu, T. Nishikawa, B. Ohtani, A. Chen, Chemistry of Materials 19 (2007) 4530–4537.
- [37] C.S. Kuo, Y.H. Tseng, C.H. Huang, Y.Y. Li, Journal of Molecular Catalysis A: Chemical 270 (2007) 93–100.
- [38] X. Yang, C. Cao, K.L. Hohn, L.E. Erickson, R. Maghirang, D. Hamal, K. Klabunde, Journal of Catalysis 252 (2007) 296–302.
- [39] Q. Xiao, L.L. Ouyang, Chemical Engineering Journal 148 (2009) 248–253.
- [40] Y. Huang, W.K. Ho, S.C. Lee, L.Z. Zhang, G.S. Li, J.C. Yu, Langmuir 24 (2008) 3510–3516.
- [41] Y. Park, W. Kim, H. Park, T. Tachikawa, T. Majima, W. Choi, Applied Catalysis B: Environmental 91 (2009) 355–361.
- [42] J.G. Yu, Y.R. Su, B. Cheng, Advanced Functional Materials 17 (2007) 1984–1990.
- [43] W. Ren, Z. Ai, F. Jia, L. Zhang, X. Fan, Z. Zou, Applied Catalysis B: Environmental 69 (2007) 138–144.
- [44] G. Yang, T. Xiao, J. Sloan, G. Li, Z. Yan, Chemistry A European Journal 17 (2011) 1096–1100.
- [45] J.L. Gole, J.D. Stout, C. Burda, Y. Lou, X. Chen, Journal of Physical Chemistry B 108 (2004) 1230–1240.
- [46] C. Cantau, T. Pigot, J.C. Dupin, S. Lacombe, Journal of Photochemistry and Photobiology A: Chemistry 216 (2010) 201–208.
- [47] D.G. Shchukin, E. Skorb, V. Belova, H. Möhwald, Advanced Materials 23 (2011) 1922–1934.
- [48] K. Prasad, D.V. Pinjari, A.B. Pandit, S.T. Mhaske, Ultrasonics Sonochemistry 17 (2010) 409–415.
- [49] L. González-Reyes, I. Hernández-Pérez, L. Díaz-Barriga Arceo, H. Dorantes-Rosales, E. Arce-Estrada, R. Suárez-Parra, J. Cruz-Rivera, Journal of Materials Science and Engineering B 175 (2010) 9–13.
- [50] S.C. Lee, H.U. Lee, S.M. Lee, G. Lee, W.G. Hong, J. Lee, H.J. Kim, Materials Letters 79 (2012) 191–194.
- [51] H.U. Lee, K. Ahn, S.Y. Jeong, C.R. Cho, J.P. Kim, J.S. Bae, H.G. Kim, S.H. Kwon, H.W. Lee, Applied Physics Letters 97 (2010) 223111 (1–3).
- [52] H. Kong, J. Song, J. Jang, Environmental Science and Technology 44 (2010) 5672–5676.
- [53] J. Ren, W. Wang, S. Sun, L. Zhang, L. Wang, J. Chang, Industrial and Engineering Chemistry Research 50 (2011) 10366–10369.
- [54] D.B. Hamal, J.A. Haggstrom, G.L. Marchin, M.A. Ikenberry, K. Hohn, K.J. Klabunde, Langmuir 26 (2010) 2805–2810.
- [55] A.L. Patterson, Physical Review 56 (1939) 978–982.
- [56] Z.B. Wu, F. Dong, W.R. Zhao, S. Guo, Journal of Hazardous Materials 157 (2008) 57–63.
- [57] H. Wang, Z. Wu, Y. Liu, Journal of Physical Chemistry C 113 (2009) 13317–13324.
- [58] D.M. Chen, Z.Y. Jiang, J.Q. Geng, Q. Wang, D. Yang, Industrial and Engineering Chemistry Research 46 (2007) 2741–2746.
- [59] F. Dong, W. Zhao, Z. Wu, Nanotechnology 19 (2008) 365607 (1–10).
- [60] J.H. Xu, J.X. Li, W.L. Dai, Y. Cao, H.X. Li, K.N. Fan, Applied Catalysis B: Environmental 79 (2008) 72–80.
- [61] W.K. Ho, J.C. Yu, S.C. Lee, Journal of Solid State Chemistry 179 (2006) 1171–1176.
- [62] J.C. Yu, W.K. Ho, J.G. Yu, H. Yip, P.K. Wong, J.C. Zhao, Environmental Science and Technology 39 (2005) 1175–1179.
- [63] J.C. Yu, J.G. Yu, W.K. Ho, Z.T. Jiang, L.Z. Zhang, Chemistry of Materials 14 (2002) 3808–3816.
- [64] J.L. Zhang, Y. Hu, M. Matsuoka, H. Yamashita, M. Minagawa, H. Hidaka, M. Anpo, Journal of Physical Chemistry B 105 (2001) 8395–8398.
- [65] K. Lee, D. Kim, P. Roy, I. Paramasivam, B.I. Birajdar, E. Spiecker, P. Schmuki, Journal of the American Chemical Society 132 (2010) 1478–1479.
- [66] D.S. Kim, S.Y. Kwak, Applied Catalysis A: General 323 (2007) 110–118.
- [67] T.M. Tsai, H.H. Chang, K.C. Chang, Y.L. Liu, C.C. Tseng, Journal of Chemical Technology and Biotechnology 85 (2010) 1642–1653.
- [68] N. Wu, J. Wang, D.N. Tafen, H. Wang, J.G. Zheng, J.P. Lewis, X. Liu, S.S. Leonard, A. Manivannan, Journal of the American Chemical Society 132 (2010) 6679–6685.
- [69] G.K. Mor, O.K. Varghese, M. Paulose, K. Shankar, C.A. Grimes, Solar Energy Materials and Solar Cells 90 (2006) 2011–2075.